

RESEARCH ARTICLE

Matrix Persymmetry Analysis for Misalignment and Foreign Object Detection in Resonant Capacitive Power Transfer

CHRISTIAN HERPERS^{ID}, (Graduate Student Member, IEEE),
AND CHRIS D. ROUSE^{ID}, (Member, IEEE)

Faculty of Engineering, University of New Brunswick, Fredericton, NB E3B 5A3, Canada

Corresponding author: Christian Herpers (christian.herpers@unb.ca)

This work was supported in part by the Natural Sciences and Engineering Research Council of Canada (NSERC) under Grant RGPIN-2023-05914 and in part by the New Brunswick Innovation Foundation (NBIF).

ABSTRACT This paper introduces a persymmetry evaluation of capacitance matrices for resonant capacitive power transfer. Persymmetry analysis of the capacitance matrix indicates imbalances and allows for distinction between misalignments and foreign objects. Misalignment and foreign object detection are achieved with a parameter-based method. Voltages on the transmitter side of a resonant capacitive power transfer link are leveraged for detection. Simulations and supporting measurements were performed with a 13.56 MHz resonant capacitive power transfer link incorporating a six-plate structure for electric vehicle charging applications. Metallic and living tissue objects can be detected with the foreign object detection method. Furthermore, lateral misalignment and its direction are detectable for realignment purposes. Simulations show that the foreign object detection range is sufficient to avoid exceeding the basic restrictions for electromagnetic field exposure for kW-range power transmission. The capacitance matrix persymmetry results indicate that both lateral misalignment and foreign object detection are achievable and distinguishable with the parameter-based method. This work introduces practical solutions to detecting imbalances in resonant capacitive power transfer systems, which may improve reliability and safety in applications such as electric vehicle charging and electrified roadways.

INDEX TERMS Capacitance matrix persymmetry, electric vehicle charging, foreign object detection, misalignment detection, resonant capacitive power transfer, wireless power transfer.

I. INTRODUCTION

Wireless power transfer (WPT) has gained interest in recent years due to an increase in mobile electronic devices. Charging these devices is necessary for continuous operation. WPT offers a convenient and autonomous way to charge that may also increase safety in high-power applications such as electric vehicles (EVs) [1], [2], [3]. Furthermore, continuous charging of EVs while driving on electrified roadways has been proposed [3]. Most research in near-field WPT has focused on inductive power transfer (IPT), which is based on magnetic field coupling [1], [2], [4]. Capacitive power transfer (CPT) uses electric field coupling [1], [4].

The associate editor coordinating the review of this manuscript and approving it for publication was Alon Kuperman^{ID}.

CPT is an emerging research topic due to its advantages over IPT. Neither expensive ferrites nor Litz wires are needed [4], [5], [6], [7]. Also, lossy eddy currents in nearby metal generated from alternating magnetic fields can be avoided in CPT [7], [8]. Finally, CPT works best at higher frequencies, which can decrease the size and mass of lumped elements [5], [9], [10].

Fig. 1 shows a simplified block diagram of a CPT system with the wireless link in the centre, an inverter on the transmit side, and a rectifier on the receive side. Resonant CPT (RCPT) is achieved when both sides of the wireless link are self-resonant at the operating frequency, e.g., via inductors [4], [7], [10]. This is advantageous when low coupling between transmitter and receiver exists, e.g., due to large air gaps in EV charging [1], [4].

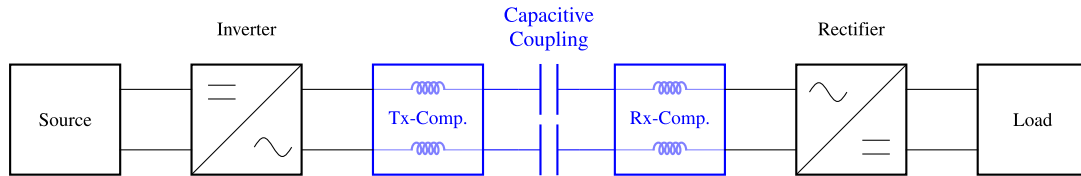


FIGURE 1. Simplified RCPT system block diagram with a capacitive wireless link [11].

Misalignment of the receiver and transmitter in both IPT and CPT can lead to reduced efficiency [5], [7], [11], [12], [13], [14], [15]. In CPT, misalignment can cause imbalances in the wireless link and undesirable common-mode currents [4], [11], [15]. Some forms of misalignment may impact the link more dominantly than others [7], [11], [14], [16], [17]. Lateral misalignment is particularly harmful to the balance [5], [11], [16], [17] and can occur easily in electrified roadways, e.g., when an EV drifts from the centre of the lane.

Foreign objects, including metal objects, may also detune the link and introduce imbalances [5], [18], [19]. When foreign objects are close to an RCPT link, they may alter the coupling, resulting in a shifted resonant frequency [19], [20] and an imbalanced system [5], [11]. This leads to reduced system performance and efficiency. If the alteration is too severe, the system can exhibit harmful common-mode currents which may damage the RCPT system [4]. Further, in the scenario of a living (tissue) object, such as an animal or a human hand, exposure to electromagnetic fields (EMFs) emitted from the CPT system is a safety concern [1], [5], [18], [21]. Standards for EMF exposure must be met to ensure safe operation [22], [23]. If a living object is too close to the link, meaning the exposure to EMFs is too high, the system must power down. Hence, foreign object detection (FOD) systems must be part of any high-power CPT implementation.

Most FOD methods were designed for IPT systems [5], [19], [21], [24], [25]. Often, they can be categorized into external sensor-based, such as thermal imaging or radar, and parameter-based, such as impedance or quality factor measurement [21], [25]. Parameter-based FOD methods do not require external circuitry, and parameter variations are measured to identify the presence of foreign objects. Some IPT FOD methods also propose additional plates to measure capacitive changes when a foreign object is present [25], [26]. Research in IPT has shown that misalignment can lead to errors in parameter-based FOD [12], [13], [27]. The impact of foreign objects and misalignment in CPT systems has been studied; however, CPT-specific misalignment detection and FOD methods have yet to be explored [5], [11], [19], [21].

This paper proposes a novel CPT-specific parameter-based FOD method for living and metallic objects. Moreover, lateral misalignment can be detected using the same method. The impact of different misalignments along with the combination of lateral misalignment and foreign objects is also studied.

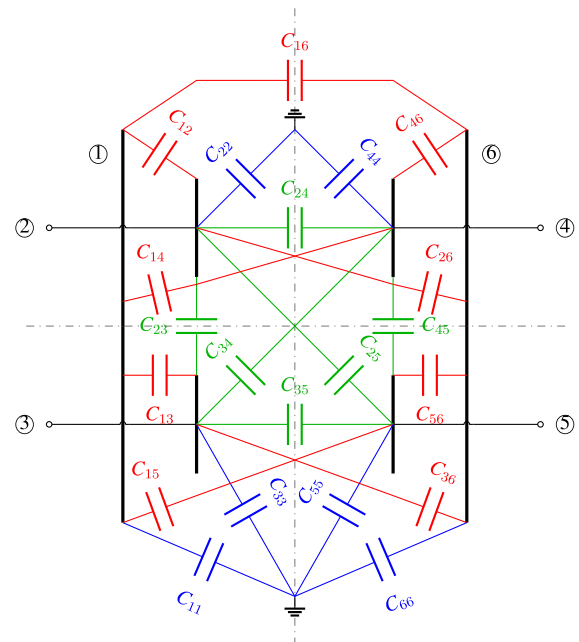


FIGURE 2. Visualization of the six-plate structure with self- and mutual capacitances [11].

The capacitance matrix provides information to detect and differentiate lateral misalignment and foreign objects. The most practically measurable voltages on the transmitter side are chosen to achieve detection in a real RCPT system.

Whereas the detection method was proposed in the underlying conference publication [5], the evaluation of symmetries in the capacitance matrix and FOD measurements validating the simulations are new contributions. Furthermore, the relationship between capacitance matrix persymmetry and RCPT system imbalances is explored in this work.

In Section II, the capacitance matrix and its symmetry patterns are presented. Section III introduces the CPT measurement and simulation setup, as well as the circuit theory approach. The simulation and measurement results for lateral misalignment and FOD are found in Section IV. Finally, Section V summarizes the results and provides an outlook to possible further research.

II. CAPACITANCE MATRICES

The capacitances of a six-plate structure CPT link are shown in Fig. 2. Common models only assess the green capacitances

originating from a four-plate structure and some research includes the red capacitances to the shields [16], [20]. In this model, self-capacitances to ground, here shown in blue, are considered as they provide undesirable common-mode return paths [4]. Electrostatic simulations can yield capacitance matrices [28]. These capacitance matrices are directly influenced by misalignment and the presence of foreign objects.

The capacitance matrix \mathbf{C} is square and symmetric due to reciprocity ($C_{mn} = C_{nm}$) [4], [28]. This matrix also exhibits persymmetry, i.e., symmetry about the secondary diagonal, under certain plate numbering schemes, so long as the transmitter and receiver are aligned and no foreign objects are present. The secondary diagonal goes from the bottom left to the top right of the matrix. Furthermore, the combination of symmetry and persymmetry results in a bisymmetric and also a centrosymmetric matrix [11]. Eq. (1), as shown at the bottom of the page.

A centrosymmetric matrix is symmetric around the centre of the matrix. Hence, for each entry of a k -by- k matrix $a_{mn} = a_{k+1-m, k+1-n}$ is given due to centrosymmetry, and $a_{mn} = a_{k+1-n, k+1-m}$ due to persymmetry [29]. A bisymmetric matrix is a matrix that is both symmetric and persymmetric [30].

Imbalances in the capacitance matrix, e.g., due to lateral misalignment or the presence of foreign objects, would cancel the persymmetry and therefore the centrosymmetry and bisymmetry of the matrix. The symmetry of the matrix will prevail due to reciprocity. A metric h of how much symmetry or anti-/skew-symmetry the matrix exhibits is proposed by the ratio of Frobenius norms $\| \cdot \|$

$$h(\mathbf{B}) = \frac{\|\mathbf{B}_{\text{sym}}\| - \|\mathbf{B}_{\text{skew}}\|}{\|\mathbf{B}_{\text{sym}}\| + \|\mathbf{B}_{\text{skew}}\|}, \quad (2)$$

where \mathbf{B}_{sym} is the symmetric part

$$\mathbf{B}_{\text{sym}} = \frac{\mathbf{B} + \mathbf{B}^T}{2}, \quad (3)$$

$[\cdot]^T$ denotes the matrix transpose, and \mathbf{B}_{skew} is the skew-symmetric part

$$\mathbf{B}_{\text{skew}} = \frac{\mathbf{B} - \mathbf{B}^T}{2}, \quad (4)$$

of a matrix \mathbf{B} whose diagonal elements were set to zero. This was done to prevent bias in the symmetry metric that would

normally result from the non-zero diagonal elements of \mathbf{B}_{sym} , as the diagonal elements of \mathbf{B}_{skew} are always zero. By setting the diagonal elements of \mathbf{B} to zero beforehand, the metric is less biased and simpler to evaluate.

The same evaluation can be performed for perymmetry. In order to do so, the matrix must first be rotated 90° via multiplication with the exchange matrix and transposing. The exchange matrix has ones on its secondary diagonal with the rest set to zero. The persymmetry metric is denoted by $h_p(\mathbf{C})$ in the following. A purely persymmetric matrix would result in $h_p = +1$ and a purely skew-persymmetric matrix in $h_p = -1$. A more comprehensive analysis of RCPT system imbalances can be achieved by evaluating $h_p(\mathbf{C})$ for the capacitance matrix \mathbf{C} than by simply comparing the individual capacitance entries.

A new bisymmetric matrix \mathbf{C}' can be created when exchanging the ports ② & ③ and thereby the entries of the matrix (5), as shown at the bottom of the next page. The secondary diagonal now consists of the ‘‘forward capacitances’’ C_{24} & C_{35} and the ‘‘shield-to-shield capacitance’’ C_{16} . In contrast, the secondary diagonal of \mathbf{C} contains the ‘‘cross capacitances’’ C_{34} & C_{25} instead of the ‘‘forward capacitances’’ [11].

Due to the change of diagonal matrix elements, $h_p(\mathbf{C})$ and $h_p(\mathbf{C}')$ together enable a full analysis of the imbalances in the capacitance matrix.

III. SETUP AND APPROACH

The capacitance matrices of Section II are converted to lossless admittance matrices \mathbf{Y} with the angular frequency ω according to

$$\mathbf{Y} = j\omega\mathbf{C}. \quad (6)$$

Fig. 3 shows the external circuitry to the CPT link which was slightly rearranged compared to [5]. The electrode voltages to ground, $\mathbf{v} = [v_1, v_2, v_3, v_4, v_5, v_6]^T$, are related to the currents flowing into each electrode, $\mathbf{i} = [i_1, i_2, i_3, i_4, i_5, i_6]^T$, as follows:

$$\mathbf{i} = \mathbf{Y}\mathbf{v}. \quad (7)$$

Receive Y_r , transmit Y_t , and source Y_s admittances of a balanced RCPT system, as well as parasitic admittances to

$$\mathbf{C} = \begin{bmatrix} \sum_{n=1}^6 C_{1n} & -C_{12} & -C_{13} & -C_{14} & -C_{15} & -C_{16} \\ -C_{21} & \sum_{n=1}^6 C_{2n} & -C_{23} & -C_{24} & -C_{25} & -C_{26} \\ -C_{31} & -C_{32} & \sum_{n=1}^6 C_{3n} & -C_{34} & -C_{35} & -C_{36} \\ -C_{41} & -C_{42} & -C_{43} & \sum_{n=1}^6 C_{4n} & -C_{45} & -C_{46} \\ -C_{51} & -C_{52} & -C_{53} & -C_{54} & \sum_{n=1}^6 C_{5n} & -C_{56} \\ -C_{61} & -C_{62} & -C_{63} & -C_{64} & -C_{65} & \sum_{n=1}^6 C_{6n} \end{bmatrix}. \quad (1)$$

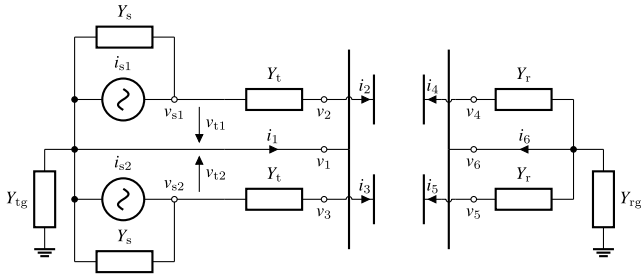


FIGURE 3. RCPT link schematics with external circuitry [5].

ground, Y_{tg} and Y_{rg} , define the augmenting matrix \mathbf{Y}_a :

$$\mathbf{Y}_a = \begin{bmatrix} -Y_{a2} & Y_{a1} & Y_{a1} & 0 & 0 & 0 \\ Y_{a1} & -Y_{a1} & 0 & 0 & 0 & 0 \\ Y_{a1} & 0 & -Y_{a1} & 0 & 0 & 0 \\ 0 & 0 & 0 & -Y_r & 0 & Y_r \\ 0 & 0 & 0 & 0 & -Y_r & Y_r \\ 0 & 0 & 0 & Y_r & Y_r & -Y_{a3} \end{bmatrix}, \quad (8)$$

where

$$Y_{a1} = \frac{Y_s Y_t}{Y_s + Y_t}, \quad (9)$$

$$Y_{a2} = Y_{tg} + 2Y_{a1}, \quad (10)$$

and

$$Y_{a3} = Y_{rg} + 2Y_r. \quad (11)$$

The resonating inductances with their quality factors are incorporated into Y_t and Y_r . Thus, i can be expressed as

$$i = i_s \frac{Y_t}{Y_s + Y_t} + \mathbf{Y}_a v, \quad (12)$$

where $i_s = [0, i_{s1}, i_{s2}, 0, 0, 0]^T$, and the system is differentially driven, i.e., $i_{s1} = -i_{s2}$. Rearranging:

$$v = (\mathbf{Y} - \mathbf{Y}_a)^{-1} i_s \frac{Y_t}{Y_s + Y_t}. \quad (13)$$

Finally, i can be obtained from (7). Thus, the transmitter voltages

$$v_{t1} = v_2 - v_1 + i_2/Y_t \quad (14)$$

and

$$v_{t2} = v_3 - v_1 + i_3/Y_t \quad (15)$$

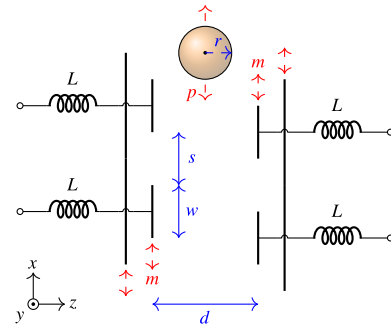


FIGURE 4. Six-plate structure RCPT link diagram under lateral misalignment and with a foreign object present [5].

can be determined. Section IV will show that these are sensitive to both lateral misalignment and the presence of foreign objects. They appear between the transmit circuitry and resonator and are therefore relatively easy to measure in practice.

The augmenting matrix \mathbf{Y}_a is also symmetric due to the symmetric drive and load circuit, and the entries are distributed persymmetrically. However, since the external circuitry is not identical on the receiver and transmitter side, neither persymmetry, centrosymmetry, nor bisymmetry are observed.

Fig. 4 shows the RCPT link from a top view. The active electrodes have a width of $w = 135$ mm and a lateral spacing of $s = 90$ mm, while the shields have a length and width of 600 mm. The air gap $d = 125$ mm was chosen as the range from 100 mm to 150 mm is common for CPT EV charging [1]. The six-plate structure was chosen as the shields reduce EMF emissions [17]. Inductors L as seen in Fig. 4 were designed as part of a split-L compensation network. The air core copper foil inductor realizations can be seen on the left side in Fig. 5. The inductor design of Regensburger et al. [31] was leveraged to simulate and build the inductors. Lateral misalignment in x -direction is denoted by m . A spherical foreign object with a radius r has a position p in x -direction. The RCPT link was designed for high-power applications in the industrial, scientific, and medical band of 13.56 MHz, as CPT can outperform IPT for frequencies above 10 MHz [9].

Metallic foreign objects were simulated in CST Studio Suite as perfect electric conductor (PEC) and substituted with

$$\mathbf{C}' = \begin{bmatrix} \sum_{n=1}^6 C_{1n} & -C_{13} & -C_{12} & -C_{14} & -C_{15} & -C_{16} \\ -C_{31} & \sum_{n=1}^6 C_{3n} & -C_{32} & -C_{34} & -C_{35} & -C_{36} \\ -C_{21} & -C_{23} & \sum_{n=1}^6 C_{2n} & -C_{24} & -C_{25} & -C_{26} \\ -C_{41} & -C_{43} & -C_{42} & \sum_{n=1}^6 C_{4n} & -C_{45} & -C_{46} \\ -C_{51} & -C_{53} & -C_{52} & -C_{54} & \sum_{n=1}^6 C_{5n} & -C_{56} \\ -C_{61} & -C_{63} & -C_{62} & -C_{64} & -C_{65} & \sum_{n=1}^6 C_{6n} \end{bmatrix} \quad (5)$$

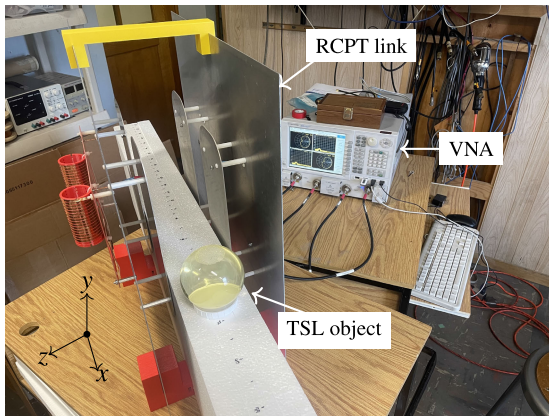


FIGURE 5. Measurement setup for FOD with a TSL HBBL4-250V3 sphere.

aluminum in measurements. For living objects, a homogeneous mass consisting of a tissue equivalent medium with a conductivity of 0.75 S/m, a density of 1 g/cm³, and a relative permittivity of 55 was assumed for frequencies from 4 MHz to 30 MHz according to [32].

In the laboratory setup, tissue simulating liquid (TSL) HBBL4-250V3 with a relative permittivity of 54.4, a density of 1.042 g/cm³ and a conductivity of 0.73 S/m was used. These values were targeted and measured by the manufacturer (Schmid & Partner Engineering AG) in accordance with [32]. Fig. 5 shows the RCPT link measurement setup during measurement with a 50 mm radius TSL sphere and an Agilent N5242A vector network analyzer (VNA). All electrodes were made from aluminum to reduce weight. Active electrodes made from copper instead of aluminum were tested but did not impact the system parameters. In both cases, an RCPT link efficiency of approximately 96% was measured [5], [11]. Scattering parameters from the VNA and the differential source currents were used to determine the transmitter voltages. Measurements were conducted with a VNA instead of a resonant inverter and rectifier. These could be damaged by increased current stress due to imbalances created under lateral misalignment or the presence of a foreign object, which give rise to common-mode currents [4]. As the capacitive link and the compensation stages are purely passive, linearity is assumed. Hence, low-power measurements with a VNA give accurate results on the behaviour of the capacitive link.

Multiple types of misalignments can exist in a CPT link [1]. In a practical scenario, the receiver as a mobile device can be translated into three directions (e.g., x , y , z) and can rotate about the same three axes. Furthermore, an arbitrary combination of these can occur. Fig. 6 shows the individual types of misalignments. On an electrified roadway, medial alignment (Fig. 6c) will happen due to an EV travelling down the road, in y -direction. Lateral misalignment (Fig. 6a) can occur when an EV is not centred in the lane. Tilting (Fig. 6b), angular (Fig. 6d), as well as vertical (Fig. 6e) misalignment

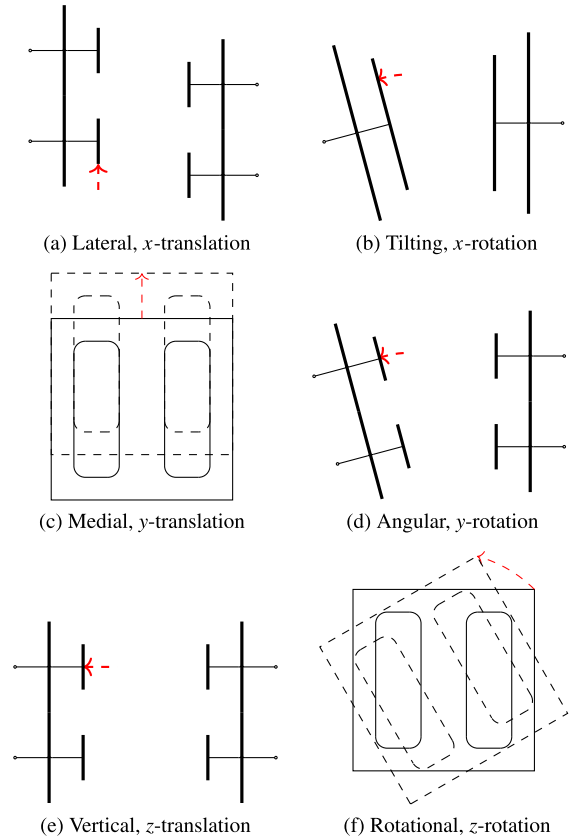


FIGURE 6. Misalignment types for a six-plate structure CPT link [11].

TABLE 1. Simulation settings for misalignment.

Type	Axis	Rot/transl	Range	Step width
lateral	x	translation	± 250 mm	10 mm
tilting	x	rotation	$\pm 45^\circ$	2.5°
medial	y	translation	± 300 mm	10 mm
angular	y	rotation	$\pm 45^\circ$	2.5°
vertical	z	translation	± 50 mm	5 mm
rotational	z	rotation	$\pm 90^\circ$	5°

may happen due to uneven roads or tire pressure and load of an EV. Rotational misalignment (Fig. 6f) could occur while turning or when being parked.

IV. SIMULATION AND MEASUREMENT RESULTS

A. CAPACITANCE MATRIX PERSYMMETRY

All six types of misalignments from Fig. 6 were evaluated. Table 1 shows the settings for each misalignment simulation in the electrostatic solver of CST Studio Suite. In the simulations the receiver was moved linearly over the range with the set step width. Under alignment and without any foreign object being present, the simulated six-plate structure exhibited the capacitance values listed in Table 2.

The resulting capacitance matrices were assessed based on their score for persymmetry h_p with (2). Fig. 7a shows the results for the matrix constellation C and Fig. 7b

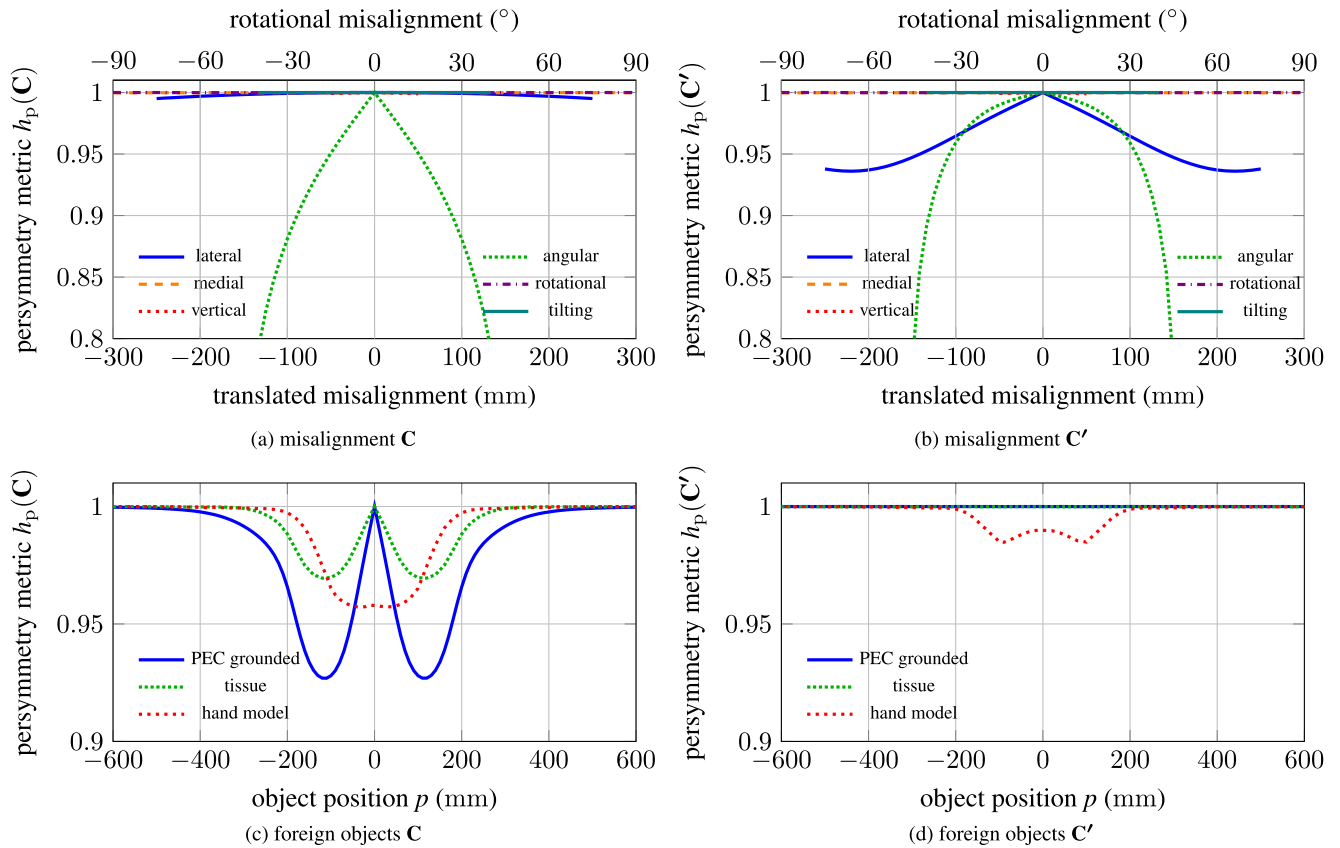


FIGURE 7. Persymmetry metric h_p evaluation for misalignment and foreign objects with matrix constellations \mathbf{C} and \mathbf{C}' [11]. (a) misalignment \mathbf{C} (b) misalignment \mathbf{C}' (c) foreign objects \mathbf{C} (d) foreign objects \mathbf{C}' .

TABLE 2. Self- and mutual capacitances under alignment without foreign object.

Quantity	Value	Quantity	Value
C_{11}, C_{66}	60.6 pF	$C_{12}, C_{13}, C_{46}, C_{56}$	13.9 pF
C_{34}, C_{25}	0.382 pF	$C_{14}, C_{15}, C_{26}, C_{36}$	1.47 pF
C_{23}, C_{45}	0.687 pF	$C_{22}, C_{33}, C_{44}, C_{55}$	19.8 pF
C_{24}, C_{35}	3 pF	C_{16}	9.3 pF

for the matrix constellation \mathbf{C}' . Only lateral and angular misalignment significantly impact the persymmetry. Note that lateral misalignment only has a significant impact on the persymmetry of \mathbf{C}' , not \mathbf{C} . For the remaining types of misalignments, persymmetry is still observed, even under strong misalignment. Hence, they do not imbalance the RCPT link by themselves.

The “cross-capacitances” C_{34} and C_{25} are imbalanced under lateral misalignment, but not the “forward-capacitances” C_{24} and C_{35} . Angular misalignment shows imbalance in all of them. For both lateral and angular, greater misalignment shows a higher deviation from perfect persymmetry. Lateral misalignment in Fig. 7a shows a minimum at $s + w = 225$ mm as then two opposing plates are aligned and a maximum imbalance between C_{34} and C_{25} is reached.

The persymmetries of the same matrix constellations were evaluated in the presence of foreign objects. The object was moved through the centre of the RCPT link along x -direction as indicated in Fig. 4 and Fig. 5. Both PEC and TSL spheres with radii of $r = 50$ mm as well as a hand model with TSL were simulated. Here, the PEC sphere’s potential is assumed grounded. The outcomes are plotted in for $h_p(\mathbf{C})$ in Fig. 7c and $h_p(\mathbf{C}')$ in Fig. 7d. The spherical foreign objects show perfect persymmetry for $h_p(\mathbf{C}')$ but deviate from persymmetry for $h_p(\mathbf{C})$. As the spheres themselves are symmetric, persymmetry is given when they are in the centre of the link at $p = 0$. The foreign objects imbalance the “forward-capacitances” C_{24} and C_{35} more than the “cross-capacitances” C_{34} and C_{25} . Hence, the behaviour of the foreign objects is opposite to lateral misalignment. The hand model itself is not symmetric and therefore $h_p(\mathbf{C}')$ is not always one, however $h_p(\mathbf{C})$ is more sensitive to it. By comparing the persymmetry metrics of both matrix constellations $h_p(\mathbf{C}')$ and $h_p(\mathbf{C})$, lateral misalignment and foreign objects can be distinguished from one another.

Both lateral misalignment and foreign objects were simulated simultaneously. Fig. 8 shows the simulation results for the persymmetry metrics for both matrix constellations with a TSL object. Vertical cross sections from Fig. 8a resemble the spherical object results from Fig. 7c, with

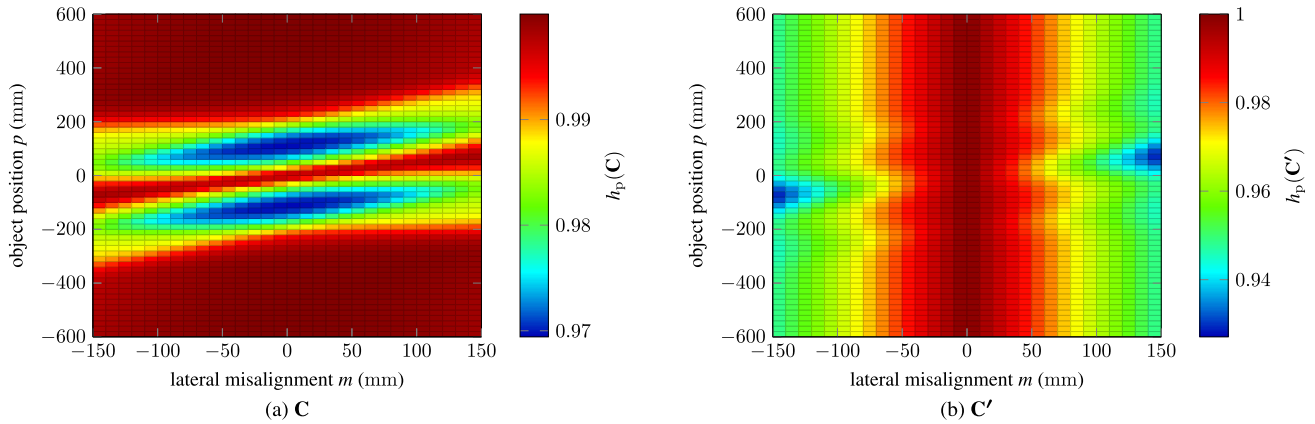


FIGURE 8. Persymmetry metric h_p evaluation for combined misalignment and foreign spherical TSL object with matrix constellations (a) C (b) C' [11].

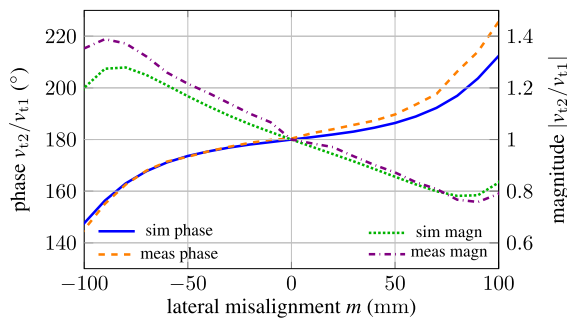


FIGURE 9. Lateral misalignment detection simulation and measurement combined results [5].

perfect persymmetry when the foreign object is in the centre of and far away from the RCPT link. Note that the centre of the RCPT link shifts with $m/2$ when the receiver is misaligned relative to the transmitter. This creates the slight diagonal behaviour in Fig. 8a. Horizontal cross sections from Fig. 8b resemble the lateral misalignment results from Fig. 7b. Here persymmetry is given for no lateral misalignment, $m = 0$, regardless of the foreign object position p . Simulations with a PEC instead of a TSL object show nearly identical results when the PEC object is floating. With non-symmetrical objects such as the hand model from Fig. 7c the results would be less clear. However, with all tested foreign objects the imbalance on “forward-capacitances” C_{24} and C_{35} dominates, compared to “cross-capacitances” C_{34} and C_{25} . These results in Fig. 8 clearly indicate that FOD can be performed under lateral misalignment. Further, the two can be differentiated from each other by evaluating h_p for both matrix constellations.

B. LATERAL MISALIGNMENT DETECTION

In a scenario such as an electrified roadway, an EV as receiver may drift from the centre of the lane, making it laterally misaligned with the transmitter. Lateral misalignment as shown in Fig. 7 will imbalance the RCPT link more significantly than other types of non-angular misalignments.

Hence, the detection of lateral misalignment may be a valuable improvement in the reliability of an RCPT system. This sensitivity in the capacitance matrix may be used for the detection of lateral misalignment. With the analysis presented in Section III, the transmitter voltages can be determined via (14) and (15). These transmitter voltages change when imbalances are present, resulting in a reduced voltage under constant resistance loading [5]. Simulation and measurement results are shown in Fig. 9 for a loaded receiver and they compare well. Slight deviations occur because the feed wires and printed circuit boards are not fully included in the simulation model. Their effects are estimated and incorporated in the augmenting matrix Y_a . While the VNA measurements are precise, manual misalignment is less exact. The transmitter voltage ratio v_{t2}/v_{t1} was used to generate a function with odd symmetry over a misalignment range of ± 100 mm. With this the direction and extent of misalignment can be determined, providing feedback to enable precise realignment of the receiver, e.g., on an EV.

C. FOREIGN OBJECT DETECTION

The same transmitter voltages are analyzed with foreign objects present and the receiver being unloaded. The unloaded or open receiver would mimic a scenario before power transfer is initiated. For simulation results, the same capacitance matrices were used as in Fig. 7c and Fig. 7d. The measurement results were created with the setup in Fig. 5. Magnitude and phase information are shown in Fig. 10a and Fig. 10b, respectively, for a TSL object with $r = 50$ mm. The same was performed for the metallic spheres (PEC in simulation and aluminum in measurements). With the object close or within the RCPT link the voltage magnitudes rise and the phases deviate from their original state at 0° and 180° . The voltage magnitude does not reach zero, even with the object far away, due to the source and ground admittances, Y_{tg} and Y_{rg} .

It can be seen that the measurements and simulations for the sphere compare well. Moreover, it was observed,

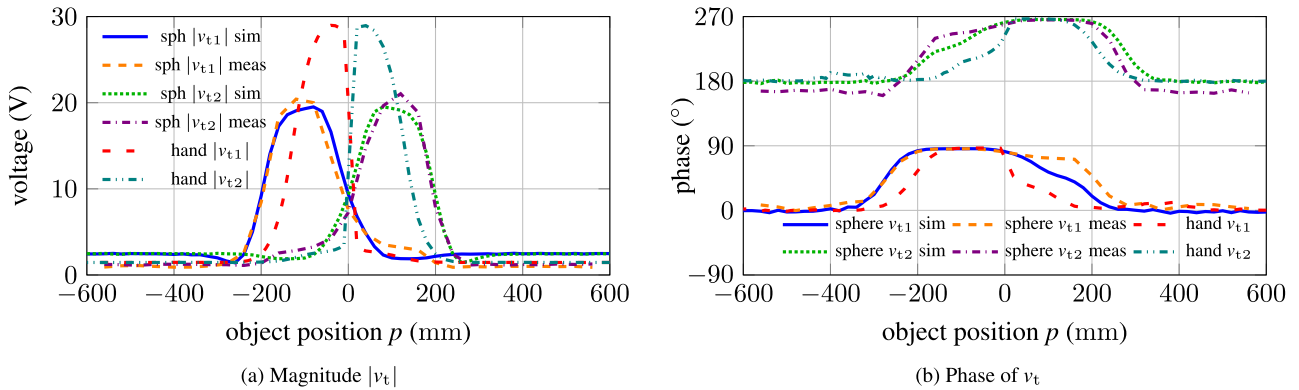


FIGURE 10. Transmitter voltages of FOD measurement and simulation results of a TSL sphere and hand model under alignment and unloaded receiver [11]. (a) magnitude (b) phase.

in simulation and measurements, that the TSL and metallic FOD results are nearly identical, as the objects were assumed to be floating in simulation. This is due to the conductivity of the TSL which is large enough to behave as a good conductor at 13.56 MHz. During the measurements, the objects were placed on polystyrene foam to ensure they were not connected to the electrodes or ground. Phase deviations can be used to detect an object. For a detection threshold of 10° deviation, the detection range for the sphere is at ± 320 mm, i.e., 20 mm beyond the shield electrodes on each side. The magnitudes could be used to identify which side of the RCPT link the object is located on. A grounded PEC sphere shows a greater response and is detected further away from the link [5], [11].

In addition to the spherical foreign objects, a homogeneous hand model with TSL was simulated. Fig. 10 shows the corresponding simulation results. Unlike the spherical foreign object, the hand model did not have a clear centre. Hence, a knuckle of the index finger was chosen as object position p , as it was closest to the centre of the RCPT link. The hand was simulated to be reaching in from both sides of the link resulting in a jump at $p = 0$. For the same detection threshold, the hand model is detectable within ± 270 mm, i.e., 30 mm within the shield electrodes on each side. The simulation model of the hand only contained a part of the forearm. An extended simulation model with more parts of the body may result in a greater detection range.

Measurements with a loaded receiver were also performed and compared to simulation results. A loaded receiver would mimic a scenario during power transmission. Fig. 11 shows the magnitude transmitter voltage results for the same metallic spheres. The results for the TSL sphere were nearly identical and therefore not plotted. As the simulations do not include parasitics from the feeds and printed circuit boards the absolute values differ. Normalization at $p = 600$ mm, where the object is furthest away, was chosen. The phase information is no longer useful for detection in a loaded scenario. However, the magnitude deviation may be used as

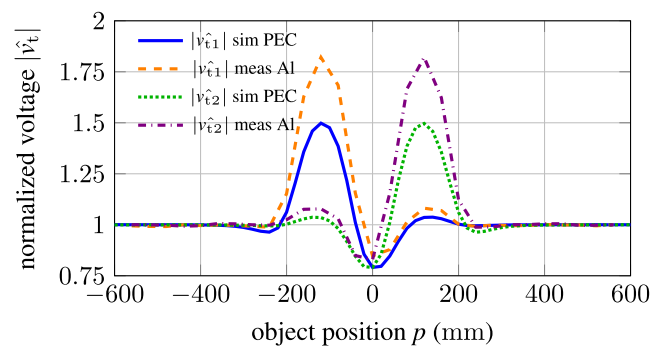


FIGURE 11. Transmitter voltage magnitudes of metallic sphere FOD measurement and simulation results under alignment and optimally loaded receiver [11].

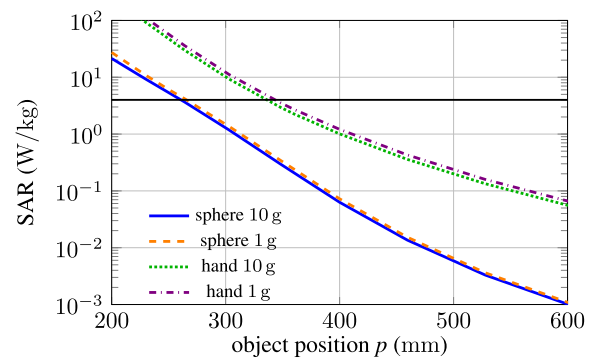


FIGURE 12. SAR simulation results for a spherical tissue object [5] and a hand model [11] averaged over 1 g and 10 g at 10 kW.

an indicator. Compared to an unloaded receiver, the detection range would be less.

The simulation and measurement results correspond well in the case of misalignment and for the different objects and loads. This further validates the model presented in Section III, Fig. 3, and [5], [11]. The introduction of the capacitance matrix with self-capacitances in RCPT for all electrodes [4], [5] is found to be a more accurate model.

D. SAR EVALUATION

The detection ranges for spherical objects were put into perspective in terms of specific energy absorption rate (SAR) in [5]. Here, the SAR simulation results for the hand model are also included. As in [5] and [11], CST Studio Suite was used to evaluate the SAR. Fig. 12 shows the 10 g and 1 g peak spatial averaged SAR for an exemplary transmitted power of 10 kW with an optimally loaded receiver. Recent CPT systems report power levels in the kilowatt range [1], [17], [31]. The hand model shows a higher SAR than the spheres due to the more exposed fingers [11]. The simulated spheres would meet the International Commission for Non-Ionizing Radiation Protection (ICNIRP) guidelines [22] as presented in [5]. However, the hand model does not meet the limit of 4 W/kg for limbs [22] which is drawn in black in Fig. 12. In order to meet this limit the detection range would have to be extended to 340 mm or the transmitted power reduced to 1.6 kW [11].

V. CONCLUSION

This article presents a parameter-based FOD method for both living tissue and metal objects in RCPT systems. FOD results suggest that EMF exposure levels adhering to ICNIRP guidelines could be maintained for kW-level power transmission. Lateral misalignment can also be detected using the same method. Furthermore, the persymmetry of capacitance matrices can be analyzed to determine and differentiate sources of imbalance. Lateral misalignment and foreign objects cause imbalance for different coupling capacitances. The capacitance matrix model for RCPT was further validated through matching simulations and measurements under the influence of foreign objects. The presented approach may be used to further identify sources of imbalance in RCPT systems, and hence to ultimately resolve these imbalances with precise detection feedback.

Due to its impact on the balance of the link, lateral misalignment was a focus of this work. Future work may further investigate the effects and possible detection methods for angular or other types of misalignments. Furthermore, the capacitance matrix and its symmetry properties may be leveraged to design RCPT transmitters and receivers that are less susceptible to misalignment. Implementation of the proposed detection methods at high power would be a logical next step.

ACKNOWLEDGMENT

An earlier version of this paper was presented at the IEEE Wireless Power Technologies Conference and Expo (WPTCE), San Diego, CA, USA, June 2023 [DOI: 10.1109/WPTCE56855.2023.10215924]. This paper is based on the master's thesis [11] published through the University of New Brunswick, Fredericton, NB, Canada, in October 2023.

REFERENCES

[1] M. Z. Erel, K. C. Bayindir, M. T. Aydemir, S. K. Chaudhary, and J. M. Guerrero, "A comprehensive review on wireless capacitive power transfer technology: Fundamentals and applications," *IEEE Access*, vol. 10, pp. 3116–3143, 2022.

[2] Z. Zhang, H. Pang, A. Georgiadis, and C. Cecati, "Wireless power transfer—An overview," *IEEE Trans. Ind. Electron.*, vol. 66, no. 2, pp. 1044–1058, Feb. 2019.

[3] H. Zhang, F. Lu, and C. Mi, "An electric roadway system leveraging dynamic capacitive wireless charging: Furthering the continuous charging of electric vehicles," *IEEE Electrific. Mag.*, vol. 8, no. 2, pp. 52–60, Jun. 2020.

[4] C. D. Rouse, S. R. Cove, Y. Salami, P. Arsenaault, and A. Bartlett, "Three-phase resonant capacitive power transfer for rotary applications," *IEEE J. Emerg. Sel. Topics Power Electron.*, vol. 10, no. 1, pp. 160–169, Feb. 2022.

[5] C. Herpers and C. D. Rouse, "Lateral misalignment and foreign object detection in resonant capacitive power transfer," in *Proc. IEEE Wireless Power Technol. Conf. Expo.*, Jun. 2023, pp. 1–5.

[6] A. Kumar, S. Pervaiz, C.-K. Chang, S. Korhummel, Z. Popovic, and K. K. Afridi, "Investigation of power transfer density enhancement in large air-gap capacitive wireless power transfer systems," in *Proc. IEEE Wireless Power Transf. Conf. (WPTC)*, May 2015, pp. 1–4.

[7] A. Reatti, L. Pugi, F. Corti, and F. Grasso, "Effect of misalignment in a four plates capacitive wireless power transfer system," in *Proc. IEEE Int. Conf. Environ. Electr. Eng. IEEE Ind. Commercial Power Syst. Eur.*, Jun. 2020, pp. 1–4.

[8] Y. Zeltser, I. Zeltser, and Mor. M. Peretz, "A computer-assisted EMF emission assessment workflow for capacitive-based wireless power transfer systems," in *Proc. IEEE 23rd Workshop Control Model. Power Electron. (COMPEL)*, Jun. 2022, pp. 1–7.

[9] S. Sinha, S. Maji, and K. K. Afridi, "Comparison of large air-gap inductive and capacitive wireless power transfer systems," in *Proc. IEEE Appl. Power Electron. Conf. Expo.*, Jun. 2021, pp. 1604–1609.

[10] C. D. Rouse and A. Tahavorgar, "Multi-megahertz load independent synchronous rectifier for resonant wireless power transfer applications," in *Proc. IEEE Appl. Power Electron. Conf. Expo. (APEC)*, Mar. 2022, pp. 505–511.

[11] C. Herpers, "Detection of misalignment and foreign objects in resonant capacitive power transfer," M.S. thesis, Dept. Elect. Comput. Eng., Univ. New Brunswick, Fredericton, Canada, 2023.

[12] A. Ramezani, S. Wang, and M. Perry, "A misalignment tolerant foreign object detection for EV wireless charging applications," in *Proc. IEEE Wireless Power Technol. Conf. Expo. (WPTCE)*, Jun. 2023, pp. 1–5.

[13] B. Long, M. Han, Q. Zhu, and A. Patrick Hu, "An online metal object detection method for inductive power transfer by improved dual frequency tuning design," in *Proc. IEEE Wireless Power Technol. Conf. Expo. (WPTCE)*, Jun. 2023, pp. 1–5.

[14] T. Komaru and H. Akita, "Positional characteristics of capacitive power transfer as a resonance coupling system," in *Proc. IEEE Wireless Power Transf. (WPT)*, May 2013, pp. 218–221.

[15] C. Liu, A. P. Hu, B. Wang, and N. C. Nair, "A capacitively coupled contactless matrix charging platform with soft switched transformer control," *IEEE Trans. Ind. Electron.*, vol. 60, no. 1, pp. 249–260, Jan. 2013.

[16] S. Sinha, A. Kumar, B. Regensburger, and K. K. Afridi, "A new design approach to mitigating the effect of parasitics in capacitive wireless power transfer systems for electric vehicle charging," *IEEE Trans. Transport. Electrific.*, vol. 5, no. 4, pp. 1040–1059, Dec. 2019.

[17] H. Zhang, F. Lu, H. Hofmann, W. Liu, and C. C. Mi, "Six-plate capacitive coupler to reduce electric field emission in large air-gap capacitive power transfer," *IEEE Trans. Power Electron.*, vol. 33, no. 1, pp. 665–675, Jan. 2018.

[18] F. Lu, "High power capacitive power transfer for electric vehicle charging applications," Ph.D. dissertation, Dept. Elect. Comput. Eng., Univ. Michigan, Ann Arbor, MI, USA, 2017.

[19] R. Sarabia Soto, S. Maji, D. Etta, and K. K. Afridi, "A novel foreign object detection and classification algorithm for capacitive wireless charging systems," in *Proc. IEEE Wireless Power Technol. Conf. Expo. (WPTCE)*, Jun. 2023, pp. 1–5.

[20] B. Regensburger, A. Kumar, S. Sinha, and K. K. Afridi, "Impact of foreign objects on the performance of capacitive wireless charging systems for electric vehicles," in *Proc. IEEE Transp. Electrific. Conf. Expo. (ITEC)*, Jun. 2018, pp. 892–897.

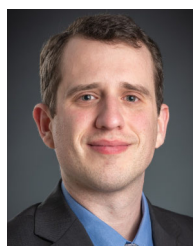
[21] J. Xia, X. Yuan, J. Li, S. Lu, X. Cui, S. Li, and L. M. Fernández-Ramírez, "Foreign object detection for electric vehicle wireless charging," *Electronics*, vol. 9, no. 5, p. 805, May 2020.

- [22] International Commission on Non-Ionizing Radiation Protection, "Guidelines for limiting exposure to electromagnetic fields (100 kHz to 300 GHz)," *Health Phys.*, vol. 118, no. 5, p. 483, 2020.
- [23] *Wireless Power Transfer for Light-Duty Plug-in/Electric Vehicles and Alignment Methodology*, Standard J2954, SAE Int., 2022.
- [24] C.-H. Jeong, P.-H. La, S.-J. Choi, and H.-S. Choi, "A novel target detection algorithm for capacitive power transfer systems," in *Proc. IEEE Appl. Power Electron. Conf. Expo. (APEC)*, Mar. 2018, pp. 3174–3177.
- [25] J. Lu, G. Zhu, and C. C. Mi, "Foreign object detection in wireless power transfer systems," *IEEE Trans. Ind. Appl.*, vol. 58, no. 1, pp. 1340–1354, Jan. 2022.
- [26] S. Y. Jeong, H. G. Kwak, G. C. Jang, and C. T. Rim, "Living object detection system based on comb pattern capacitive sensor for wireless EV chargers," in *Proc. IEEE 2nd Annu. Southern Power Electron. Conf. (SPEC)*, Dec. 2016, pp. 1–6.
- [27] S. Niu, C. Zhang, Y. Shi, S. Niu, and L. Jian, "Foreign object detection considering misalignment effect for wireless EV charging system," *ISA Trans.*, vol. 130, pp. 655–666, Nov. 2022.
- [28] S. Wengren, A. Clements, and T. Johnson, "Capacitively coupled resonator models for investigating spatial impedance variation in WPT systems," in *Proc. IEEE Wireless Power Transf. Conf. (WPTC)*, Jun. 2018, pp. 1–4.
- [29] I. S. Pressman, "Matrices with multiple symmetry properties: Applications of centrohermitian and perhermitian matrices," *Linear Algebra Appl.*, vol. 284, nos. 1–3, pp. 239–258, Nov. 1998.
- [30] A. Liao and Y. Lei, "Least-squares solutions of matrix inverse problem for bi-symmetric matrices with a submatrix constraint," *Numer. Linear Algebra Appl.*, vol. 14, no. 5, pp. 425–444, Jun. 2007.
- [31] B. Regensburger, S. Sinha, A. Kumar, S. Maji, and K. K. Afridi, "High-performance multi-MHz capacitive wireless power transfer system for EV charging utilizing interleaved-foil coupled inductors," *IEEE J. Emerg. Sel. Topics Power Electron.*, vol. 10, no. 1, pp. 35–51, Feb. 2022.
- [32] *IEC/IEEE International Standard—Measurement Procedure for the Assessment of Specific Absorption Rate of Human Exposure To Radio Frequency Fields From Hand-held and Body-mounted Wireless Communication Devices—Part 1528: Human Models, Instrumentation, and Procedures (frequency Range of 4 MHz To 10 GHz)*, Standard IEC62209–1528, 2020, pp. 1–284.



Teaching Assistant with the University of New Brunswick. His research interests include wireless power, antenna arrays, and RF engineering.

CHRISTIAN HERPERS (Graduate Student Member, IEEE) received the B.Eng. degree in electrical engineering and information technology from Munich University of Applied Sciences, Munich, Germany, in 2022, and the M.Sc.E. degree in electrical engineering from the University of New Brunswick, Fredericton, NB, Canada, in 2023. From 2017 to 2022, he was a dual and working student with Rohde and Schwarz, Munich. From 2022 to 2023, he was a Research and



Development Canada, Ottawa, ON, Canada. He is currently an Assistant Professor with the Department of Electrical and Computer Engineering, University of New Brunswick. His research interests include wireless power, RF exposure analysis, and radar.

CHRIS D. ROUSE (Member, IEEE) received the B.Sc.E. and Ph.D. degrees in electrical engineering from the University of New Brunswick, Fredericton, NB, Canada, in 2009 and 2014, respectively. From 2014 to 2016, he was a Research Fellow with Seamatica Aerospace Ltd., St. John's, NL, Canada. From 2016 to 2020, he was a Senior Electrical Researcher with Solace Power, Mount Pearl, NL, Canada. From 2020 to 2021, he was a Senior Engineer with Innovation, Science and Economic

• • •